Supplementary Information (SI) for Nanoscale.

Supplemental Materials for

Angularly robust terahertz third-harmonic generation empowered by all-dielectric nonlocal metasurfaces

Zhehao Ye[a], Yuancheng Fan[a†], Xu Ji[a], Yali Zeng[a], Chang Ding[a], Yongzheng Wen[b†], Fuli Zhang[a†]

[a]MOE Key Laboratory of Material Physics and Chemistry under Extraordinary Conditions and School of Physical Science and Technology, Northwestern Polytechnical University, Xi'an 710129, China;

[b]State Key Laboratory of New Ceramic Materials, School of Materials Science and Engineering, Tsinghua University,Beijing 100084, China.

E-mail address: phyfan@nwpu.edu.cn; wenyzheng@tsinghua.edu.cn; fuli.zhang@nwpu.edu.cn.

Contents

S1 The robustness of the Q-factor at arbitrary wavevector and fitted results

Since the Hamiltonian operator and the translation operator are a set of commuting operators, it can be proved by solving the Schrödinger equation that in the lattice with the potential field period of Λ, the electron wave function can be expressed as a periodically modulated plane wave. [1]

$$\varphi(\vec{r}) = u_p(\vec{r}) e^{i\vec{k}\cdot\vec{r}} \qquad \text{* MERGEFORMAT (S1)}$$

Where, $\vec{k}$ is the direction of the wave, $u_p(\vec{r})$ is the function with the period, and $\vec{r}$ is the position of the lattice.

When the structure with perturbation in our case, the period changes to 2Λ compared with the unperturbed one, the Bloch mode can be represented as

$$E(x) = u(x) e^{ik_x x} \qquad \text{* MERGEFORMAT (S2)}$$

Where, $u(x) = u(x+2p)$ when the structure with perturbation, and $E(x) = u'(x) e^{ik_x' x}$ for the unperturbed case.

The Brillouin zone wound be folded if the period boundary is applied on both side of the supercell consisting of two identical unit cells, the mode can be expressed as

$$E(x) = u'(x) e^{i\frac{\pi}{\Lambda}x} e^{i(k_x' - \frac{\pi}{\Lambda})x} \qquad \text{* MERGEFORMAT (S3)}$$

The equation * MERGEFORMAT (S3) can be written into another equivalent form as $u'(x)\exp(i\pi x/\Lambda)$ is also a function with a period of 2Λ.

$$\begin{gathered} u(x) = u'(x) e^{i\frac{\pi}{\Lambda}x} \\ k_x = k_x' - \frac{\pi}{\Lambda} \end{gathered} \qquad \text{* MERGEFORMAT (S4)}$$

The Q-factor is inversely proportional to the square of the coupling coefficient due to the coupled mode theory.[2]

$$Q \propto \frac{1}{\rho^2} \qquad \text{* MERGEFORMAT (S5)}$$

Where κ is the coupling coefficient which can be calculated by the product of the profiles of the mode and incident planar wave.[3]

$$\rho = \int E_{\text{mode}} E^{*}_{\text{Planar}} \mathrm{d}V$$ * MERGEFORMAT (S6)

Combing the Equation * MERGEFORMAT (S2) and the Equation * MERGEFORMAT (S5), the Equation * MERGEFORMAT (S6) is equivalent with

$$\rho = \int_{-\Lambda}^{\Lambda} u(x) e^{ik_x x} e^{-ik_x x} \mathrm{d}x = \int_{-\Lambda}^{\Lambda} u(x) \mathrm{d}x$$ * MERGEFORMAT (S7)

Because $u(x) = u(x + 2p)$ this is a function with the period 2Λ, the equation * MERGEFORMAT (S6) can be expanded by the Fourier series.

$$u(x) = p_0 + \sum_n \left[p_n \cos\left(n \frac{\pi}{\Lambda} x \right) + q_n \sin\left(n \frac{\pi}{\Lambda} x \right) \right]$$ * MERGEFORMAT (S8)

If without perturbation, combing the Equation * MERGEFORMAT (S4), the equation * MERGEFORMAT (S7) can also be written as

$$u(x) = u'(x) e^{i \frac{\pi}{\Lambda} x} = \left\{ p_0' + \sum_n \left[p_n' \cos\left(n \frac{2\pi}{\Lambda} x \right) + q_n' \sin\left(n \frac{2\pi}{\Lambda} x \right) \right] \right\} e^{i \frac{\pi}{\Lambda} x}$$ * MERGEFORMAT (S9)

Comparing the Equation * MERGEFORMAT (S8) and the Equation * MERGEFORMAT (S9), we could get

$$p_0 \mid_{\kappa = 0} = 0$$ * MERGEFORMAT (S10)

Where, α is the asymmetric parameter.

Combing the equation * MERGEFORMAT (S8) and the equation * MERGEFORMAT (S9), ρ can be expressed as

$$\rho = \int_{-\Lambda}^{\Lambda} u(x) \mathrm{d}x = 2 p_0 \Lambda$$ * MERGEFORMAT (S11)

By expanding p_0 into a Taylor series, we can get the relationship between the coupling coefficient κ and asymmetric parameter ε.

$$p_0 = p_{00} + p_{01} \kappa + \cdots$$ * MERGEFORMAT (S12)

Due to the equation * MERGEFORMAT (S10), we could know $p_{00}=0$. And due to $\kappa \in (0,1)$

$$p_0 \approx p_{01}\kappa \qquad \text{* MERGEFORMAT (S13)}$$

So, combing equation * MERGEFORMAT (S13) into equation (25)

$$\kappa = 2p_0\Lambda = 2p_{01}\kappa\Lambda \qquad \text{* MERGEFORMAT (S14)}$$

According to the equation * MERGEFORMAT (S5)

$$Q \propto \frac{1}{\rho^2} \approx \frac{1}{(2p_{01}\kappa\Lambda)^2} \qquad \text{* MERGEFORMAT (S15)}$$

Which means that $Q \propto \frac{1}{\kappa^2}$, and due to the valid of the k_x, the equation can be written as

$$Q \propto \frac{Q_0(k_x)}{\kappa^2} \qquad \text{* MERGEFORMAT (S16)}$$

Where $Q_0(k_x)$ means the Q-factor while $\kappa = 1$.

The Q-GMs the $Q_0(k_x) \approx Q_0(k_x=0) = Q_1$ in a wide wavevector range, so the Q-factor of Q-GMs can be written as

$$Q \propto \frac{Q_1}{\kappa^2} \qquad \text{* MERGEFORMAT (S17)}$$

While for the BZF-BIC, $Q_0(k_x) \approx \frac{Q_0(k_x=0)}{k^2} = \frac{Q_1}{k^2}$, which means the Q-factor of BZF-BICs corresponds to the wavevectors, the Q-factor of BZF-BICs can be written as

$$Q \propto \frac{Q_1}{k^2\kappa^2} \qquad \text{* MERGEFORMAT (S18)}$$

Considering the accidental BICs appear in the moment spaces, the equation * MERGEFORMAT (S18) can be extended as

$$Q_{BZF-BICs} = \frac{Q_1}{k^2\kappa^2} \cdot \frac{1}{(k-k_{BIC})^2} \cdot \frac{1}{(k+k_{BIC})^2} \text{* MERGEFORMAT}$$

(S19)

Where k_{BIC} denotes the wavevector where accidental BICs appear.

For Q-GMs with accidental BICs, the equation * MERGEFORMAT (S17) can be extended as

$$Q_{Q-GMs}=\frac{Q_1}{\kappa^2}\cdot\frac{1}{(k-k_{BIC})^2}\cdot\frac{1}{(k+k_{BIC})^2}$$

* MERGEFORMAT

(S20)

The fitted results can be seen in Figure S1 as follows:

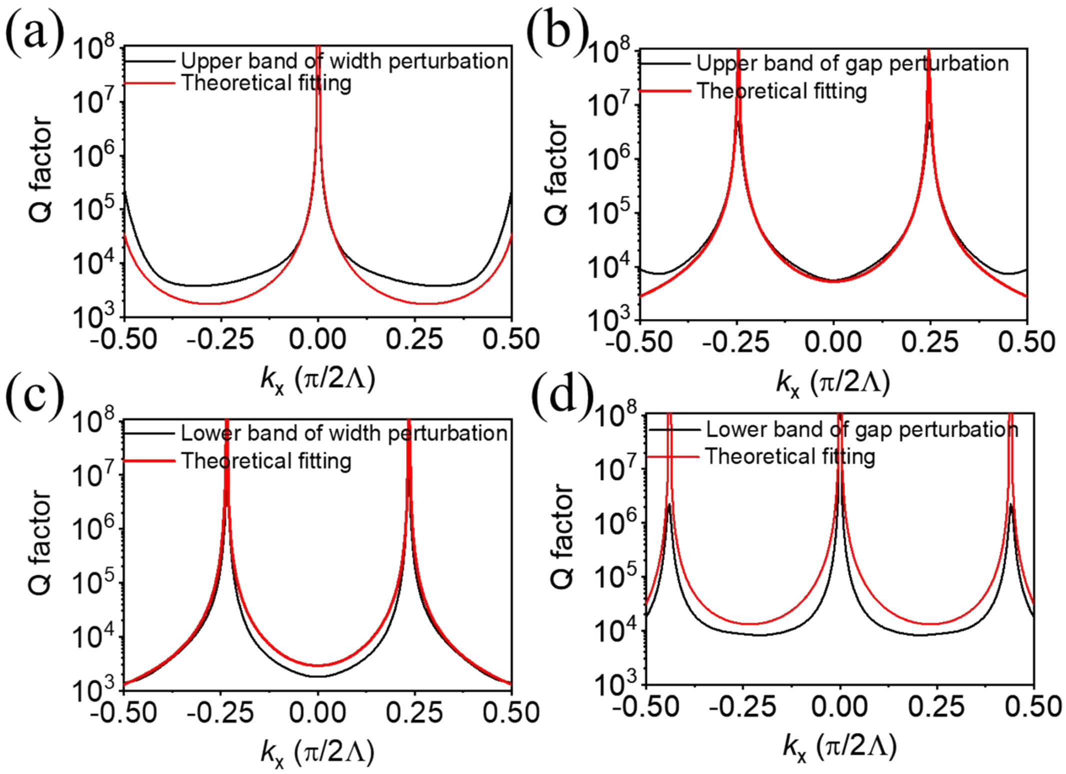

Figure S1 Fitted results of Q-GMs and BZF-BICs. (a) (c) Q factor of upper and lower band under width perturbation, respectively. (b) (d) Q factor of upper and lower band under gap perturbation, respectively.

S2. Different characteristics of period perturbation by symmetries analysis

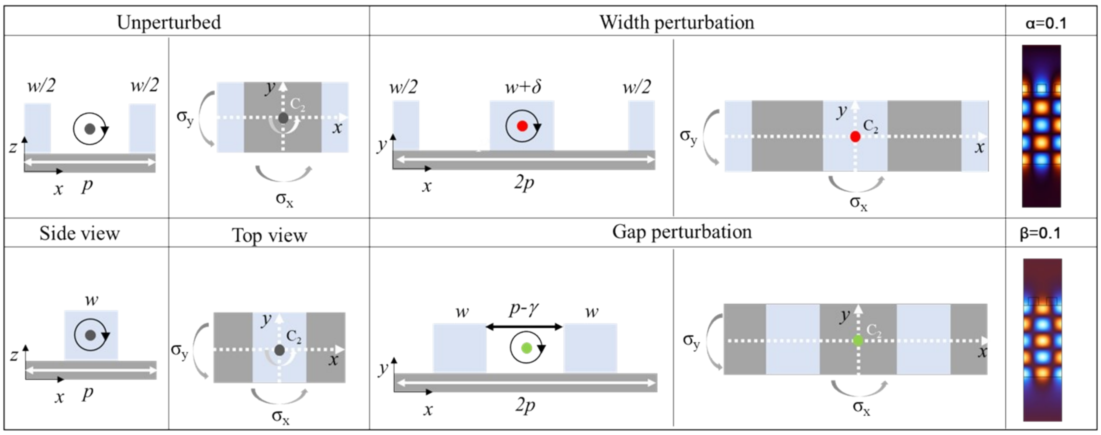

Figure S2 Symmetry operations for the unit cell of the unperturbed, width perturbation, and gap perturbation nonlocal metasurfaces.

Table S1 The character table for the C_{2v} point group

C_{2v}	E	C_2	σ_x	σ_y
A_1	1[α]	1	1	1
A_2	1	1	-1[α]	-1
B_1	1	-1	1	-1
B_2	1	-1	-1	1

[α] The numbers 1 and -1 indicate a symmetric and antisymmetric profile after applying symmetry operations, respectively.

The nonlocal metasurfaces with different symmetry operations and the irreducible representation of the modes are identified and summarized in Figure S3 and Table S1, respectively. As shown in Figure S3, for the unperturbed metasurfaces, the dielectric structure and the air gap both have A_1 irreducible representation, meaning the eigenmodes' field would also both have A_1 irreducible representation. However, when the width perturbation or the gap perturbation is induced, the Q-GMs modes would have different irreducible representations regarding different structural high symmetry points. For the case of the width perturbation, the high symmetry point is the center of the dielectric structure, represented by the red dot in Figure S3. The eigenmodes' field with width perturbation is mainly localized in the dielectric structure, as the rightest electric profile shows. While for the case of the gap perturbation, the high symmetry point is changed to the air gap between the dielectric structure, the field is mainly localized in the air.[4]

S3. The method used to obtain the far-field polarization states

The far-field polarization states are obtained by the three-dimensional simulations by the commercial software COMSOL with the eigenfrequency solver. The calculation zone in the x-y plane is a unit cell of the nonlocal metasurfaces, and the Bloch boundary conditions with the out-plane wave vector are applied as the boundary of the unit cell. In the top and bottom parts, we impose the perfectly matched layers (PML) to absorb the leaking energy of modes.[5] The eigen field ***E*** (x, y, z) is also calculated by the eigenfrequency solver, and the far-field components ***c(k)*** can be calculated by

$$c(k)=\left(c_x,c_y,c_z\right)=\frac{1}{\int_{Cell}dxdy}\int_{Cell}dxdye^{-ik_xx-ik_yy}E^*\left(x,y,z\right)\backslash *$$

MERGEFORMAT (S21)

The integration is performed above the unit cell on the x-y plane outside the metasurfaces. By sending out the TE and TM polarized plane wave with same in-plane wave vector k. we can characterize the polarization state of the far-field components ***c(k)***.

$$b^{TE}(\boldsymbol{k})=\boldsymbol{e}_{\mathrm{TE}}(\boldsymbol{k})\cdot\boldsymbol{c}\left(\boldsymbol{k}\right),\boldsymbol{e}_{\mathrm{TE}}(\boldsymbol{k})=\frac{\hat{z}\times\boldsymbol{k}}{|\hat{z}\times\boldsymbol{k}|}=\frac{1}{\sqrt{k_x^2+k_y^2}}\left(-k_y\hat{x}+k_x\hat{y}\right)\backslash *$$

MERGEFORMAT (S22)

$$b^{TM}(\boldsymbol{k})=\mathrm{e}_{TM}(\boldsymbol{k})\cdot c(\boldsymbol{k}),\quad e_{TM}(\boldsymbol{k})=\frac{k\times e_{TE}(\boldsymbol{k})}{|k\times e_{TE}(\boldsymbol{k})|}=\frac{|k|^{-1}}{\sqrt{k_x^2+k_y^2}}\left[-k_xk_z\hat{x}-k_yk_z\hat{y}+\left(k_x^2+k_y^2\right)\hat{z}\right]\backslash *$$

MERGEFORMAT (S23)

In this way, the TE plane wave with wave vector along ΓK1 direction is y-polarized.

Then, the Stokes parameters [S_0, S_1, S_2, S_3] are used to better exhibit the polarization state of the far-field with in-plane vector.[6]

$$S_0 = \left|b^{TE}(\boldsymbol{k})\right| + \left|b^{TM}(\boldsymbol{k})\right|$$ * MERGEFORMAT (S24)

$$S_1 = \left|b^{TE}(\boldsymbol{k})\right| - \left|b^{TM}(\boldsymbol{k})\right|$$ * MERGEFORMAT (S25)

$$S_2 = 2\,\mathrm{Re}\left[b^{TE*}(\boldsymbol{k})b^{TM}(\boldsymbol{k})\right]$$ * MERGEFORMAT (S26)

$$S_3 = 2\,\mathrm{Im}\left[b^{TE*}(\boldsymbol{k})b^{TM}(\boldsymbol{k})\right]$$ * MERGEFORMAT (S27)

For the position of the shell of the Poincaré sphere with the orientation angle 2ψ and ellipticity angle 2χ in Figure S4(a), the pure polarization state can be described with ψ and χ by the ellipse shown in Figure S3 (b), respectively.

$$S_0 = 1$$ * MERGEFORMAT (S28)

$$S_1 = \cos 2\chi \cos 2\psi$$ * MERGEFORMAT (S29)

$$S_2 = \cos 2\chi \sin 2\psi$$ * MERGEFORMAT (S30)

$$S_3 = \sin 2\psi$$ * MERGEFORMAT (S31)

Where ψ and χ can be calculated with

$$b_{\pm} = \left|b_{\pm}\right| e^{i\phi_{\pm}} = \frac{1}{\sqrt{2}}\left[b^{TE} \mp i b^{TM}\right]$$ * MERGEFORMAT (S32)

$$\chi = \arctan\left(\frac{\left|b_{+}\right| - \left|b_{-}\right|}{\left|b_{+}\right| + \left|b_{-}\right|}\right)$$ * MERGEFORMAT (S33)

$$\psi = \frac{\phi_{-} - \phi_{+}}{2}$$ * MERGEFORMAT (S34)

The topologic charge can be calculated by S_1 and S_2.

$$\mathrm{q} = \frac{1}{2\pi}\oint_C dk \cdot \nabla_k \phi(k)$$ * MERGEFORMAT (S35)

Where $\phi(k)$ is the azimuthal angle of the polarization state which can be defined as $\phi(k) = \frac{1}{2}\arg[S_1(k) + \mathrm{i}S_2(k)](-\pi/2 \le \phi \le \pi/2)$, and C is a simple closed path in the momentum space that winds around the BIC in the counterclockwise direction.

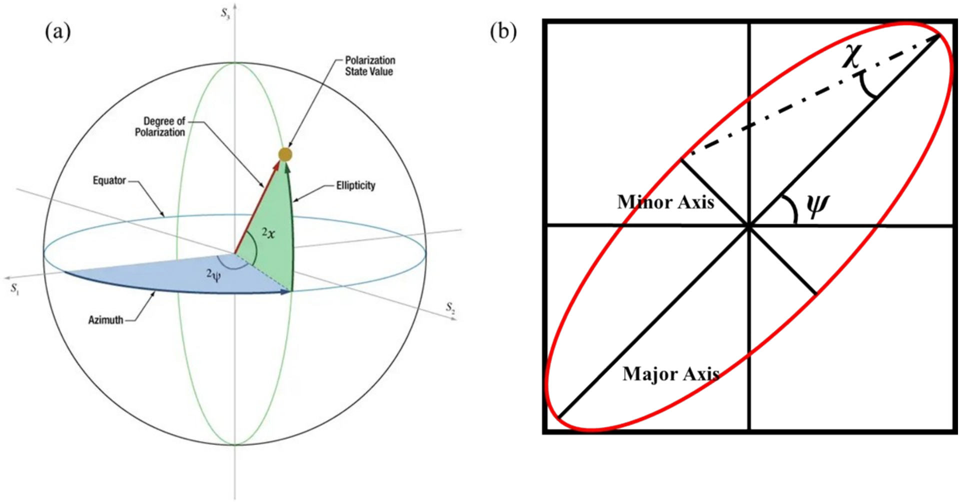

Figure S3 An exemplary diagram of polarization state representation. (a) Poincaré sphere. (b) polarization ellipse.

S4. The electromagnetic multipole decompositions

To characterize the resonance of our proposed structure, we perform the electromagnetic multipole decompositions in Cartesian coordinates to evaluate the contribution of the various multipole components to the far-field response.[7] The scattered power of multipole moments can be calculated by integrating the displacement current $J_\alpha = i\omega\varepsilon_0(\varepsilon_r - 1)E_\alpha$ over a unit cell of the nonlocal metasurfaces retrieved from the frequency domain solver, the expansion of the multiple components can be expressed as:

Electric dipole moment (ED)

$$p_\alpha = \frac{1}{i\omega}\int J_\alpha d^3r \qquad \text{* MERGEFORMAT (S36)}$$

Magnetic dipole (MD)

$$M_\alpha = \frac{1}{2c}\int (r \times J_\alpha)\mathrm{d}^3r \qquad \text{* MERGEFORMAT (S37)}$$

Toroidal dipole (TD)

$$T_\alpha = \frac{1}{10c}\int\left[(r\cdot J)r_\alpha - 2r^2J_\alpha\right]\mathrm{d}^3r \qquad \text{* MERGEFORMAT (S38)}$$

Electric quadrupole (EQ)

$$Q^{(e)}_{\alpha,\beta} = \frac{1}{2i\omega}\int\left[\left(r_\alpha J_\beta + r_\beta J_\alpha\right) - \frac{2}{3}\left(r\cdot J\right)\delta_{\alpha,\beta}\right]\mathrm{d}^3 r$$ * MERGEFORMAT

(S39)

Magnetic quadrupole (MQ)

$$Q^{(m)}_{\alpha,\beta} = \frac{1}{3c}\int\left[\left(r\times J\right)_\alpha r_\beta + \left(r\times J\right)_\beta r_\alpha\right]\mathrm{d}^3 r$$ * MERGEFORMAT

(S40)

Where ω represents the angular frequency of the resonance state, c is the speed of light in the vacuum and ***r*** specifies the location where the induced displacement current density J is evaluated and α, β =x, y, z.

The total scattering power that contribute to the far-field radiation can be obtained from the following formulas:

$$I = \frac{2\omega^4}{3c^3}\left|P\right|^2 + \frac{2\omega^4}{3c^3}\left|M\right|^2 + \frac{2\omega^6}{3c^5}\left|T\right|^2 + \frac{\omega^6}{5c^5}\sum_{\alpha,\beta}\left|Q^{(e)}_{\alpha,\beta}\right|^2 + \frac{\omega^6}{20c^5}\sum_{\alpha,\beta}\left|Q^{(m)}_{\alpha,\beta}\right|^2$$ *

MERGEFORMAT (S41)

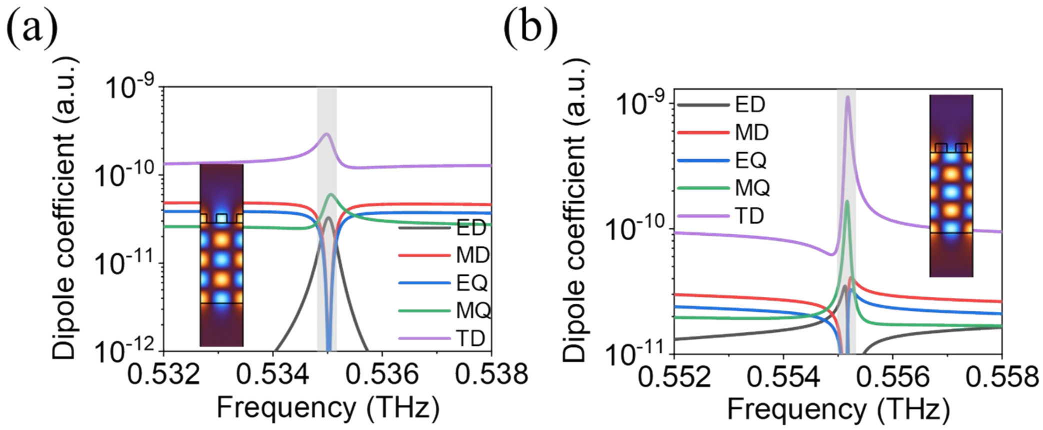

Figure S4 The electromagnetic multipole decompositions and local field. (a) The width perturbation (α=0.1). (b) The gap perturbation (β=0.1). The inserts show the local electric field parallel to the bar of the grating of the width perturbation and the gap perturbation, respectively.

The electromagnetic multipole decompositions of the Q-GMs resonances of different period perturbations are shown in Figure S4. Figure S4 (a) shows the multipoles decomposition of the width perturbation, it's obvious that the resonance around 0.535 THz is mainly caused by the TD. The local electric field parallel to the bar of the grating is shown in the insert in Figure S4 (a), indicating the electric field is mainly localized in the dielectric structure. Figure S4 (b) shows the case with gap perturbation, the Q-GMS resonance appears around 0.552 THz is also mainly caused by the TD with stronger intensity compared with that of the width perturbation. The local electric field is shown in the insert in Figure S4 (b), indicating the electric field with gap perturbation is mainly localized in the air gap. The difference between the two different period perturbations is mainly caused by different symmetry center points.

S5 Evolution of Resonance Characteristics with Asymmetry Parameters

To provide a comprehensive understanding of how the structural perturbation modulates the resonant properties, we calculated the transmission spectra and near-field distributions as a function of the asymmetry parameters (α for width perturbation and β for gap perturbation). Figure S5 illustrates the evolution of the Q-GMs. As the perturbation strength increases, a distinct broadening of the resonance linewidth is observed in the transmission color maps (Figure S5 a, c). This linewidth broadening corresponds to a decrease in the Q-factor, verifying that the radiative decay rate γ_{rad} is directly proportional to the square of the asymmetry parameter. Furthermore, the evolution of the electric field profiles (Figure S5 b, d) visually demonstrates the transition from a tightly confined mode (high-Q, under-coupled) to a leaky mode (lower-Q, over-coupled), confirming our ability to tune the system towards the critical coupling condition for optimal nonlinear efficiency.

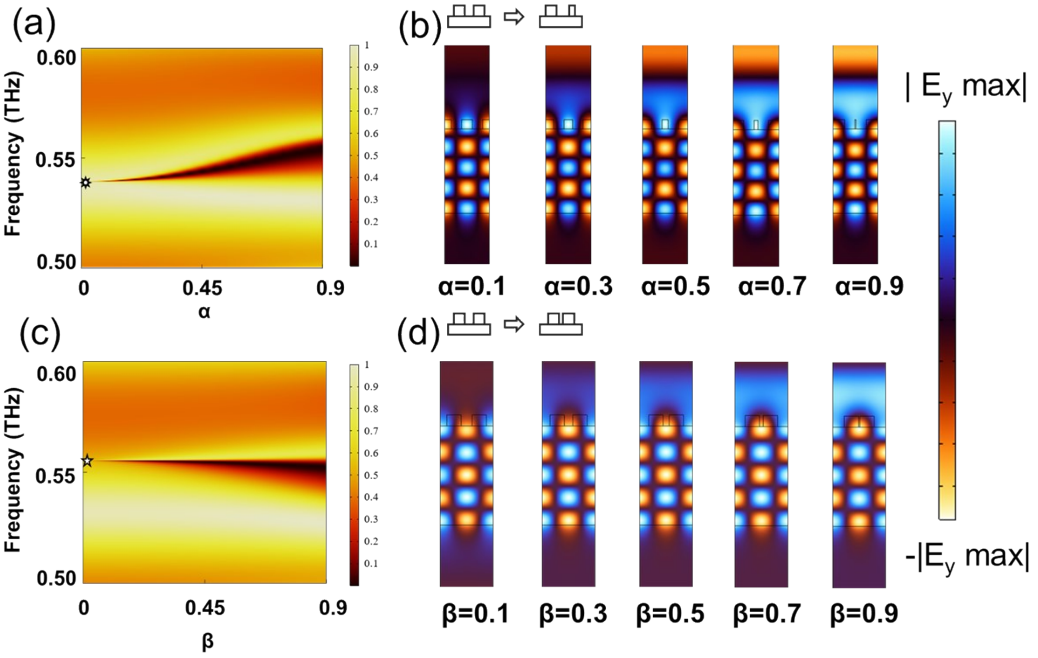

Figure S5 Evolution of transmission spectra and local electric field profiles with varying asymmetry parameters. (a, c) Calculated transmission spectra (color maps) as a function of the asymmetry parameters for width perturbation α and gap perturbation β, respectively. The resonance linewidth increases with the perturbation strength, indicating enhanced radiative leakage. Note that the width perturbation induces a noticeable blueshift in the resonance frequency, whereas the gap perturbation exhibits a relatively stable resonant frequency. (b, d) Evolution of the out-of-plane electric field distributions Ey at the Γ point corresponding to different asymmetry parameters. For small perturbations (e.g., α, β = 0.1), the field is strongly confined within the dielectric ridges. As the perturbation increases (e.g., α, β = 0.9), significant energy leakage into the free space is observed, consistent with the reduction in Q-factor.

S6. Numerical Implementation of Third-Harmonic Generation

In this work, the third-harmonic generation (THG) efficiency was numerically calculated using the Finite Element Method (FEM) in COMSOL Multiphysics. We employed a frequency-domain study with two coupled electromagnetic wave interfaces based on the undepleted pump approximation. First, a linearly polarized plane wave at the fundamental frequency was launched along the negative z-direction to excite the metasurface. Periodic boundary conditions were applied to the unit cell boundaries in the x- and y-directions. To isolate the geometric resonant enhancement effects from intrinsic material absorption, the silicon permittivity was treated as lossless in these simulations. The local electric field distribution E(ω) inside the silicon structure was then retrieved. Second, according to the nonlinear constitutive relation, the induced third-order nonlinear polarization was calculated as

$$P_{NL}^{(3)}(3\omega) = 3\varepsilon_0\chi^{(3)}(E(\omega,r)\cdot E(\omega,r))E(\omega,r)$$ *

MERGEFORMAT (S42)

Where, ε_0 denotes the permittivity in the vacuum, and $\chi^{(3)}$ denotes the third harmonic coefficient of the silicon considered isotropic with a constant value of 2.45×10^{-19} m^2/V^2 in the calculation.[8, 9] $E(\omega,r)$ denotes the local electric field. In the second electromagnetic field, we employ the $P_{NL}^{(3)}(3\omega)$ as the source of the third harmonic frequency.

This induced nonlinear polarization $P^{(3)}$ was then implemented as an external current source density $J_{ext}=i(3\omega)P^{(3)}$ in the second physics interface governing the third-harmonic frequency (3ω). The radiated power at the third harmonic (P(3ω)) was calculated by integrating the power flux (Poynting vector) at the transmission and reflection ports.

Finally, the THG conversion efficiency was defined as the ratio of the total generated third-harmonic power to the incident fundamental power.

$$\eta = \frac{P_{THG}}{P_{pump}} \qquad \text{\\* MERGEFORMAT (S43)}$$

Where, P_{THG} is the power of the third harmonic generation, and P_{pump} is the power of the pump.

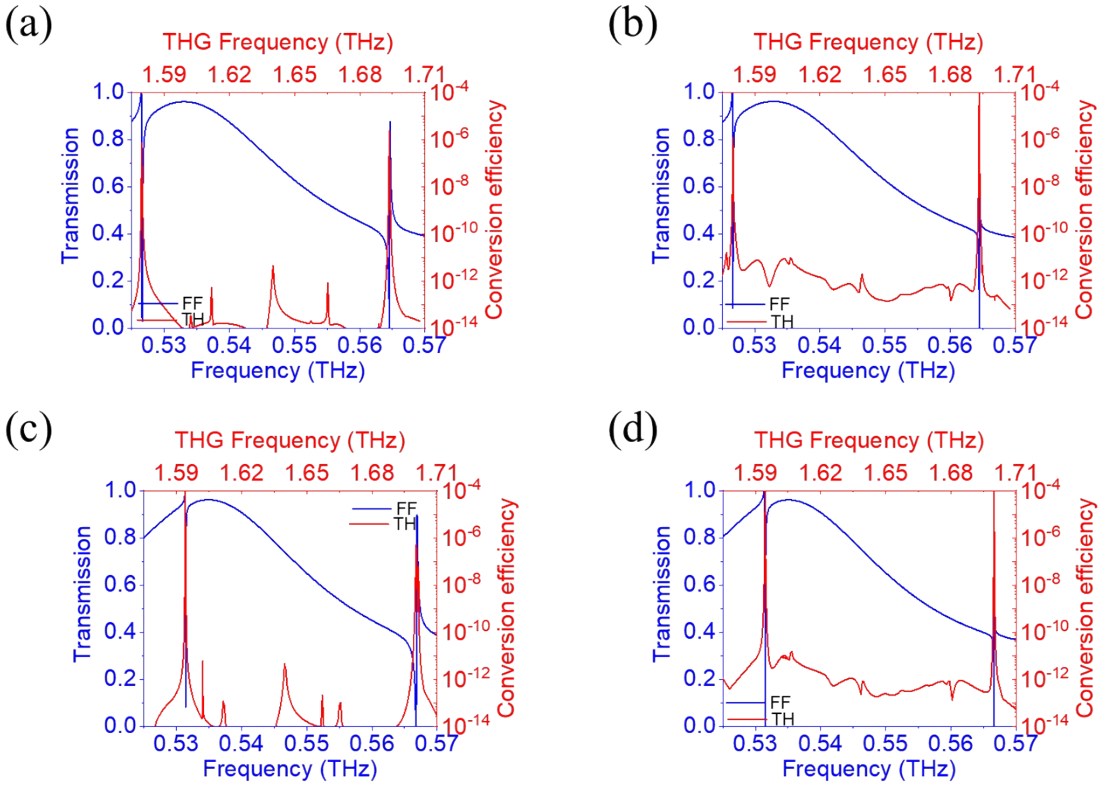

Figure S6 The conversion efficiency of THG. width perturbation with incident angle (a) 10°, (c) 20°. Gap perturbation with incident angle (b) 10° , (d) 20°.

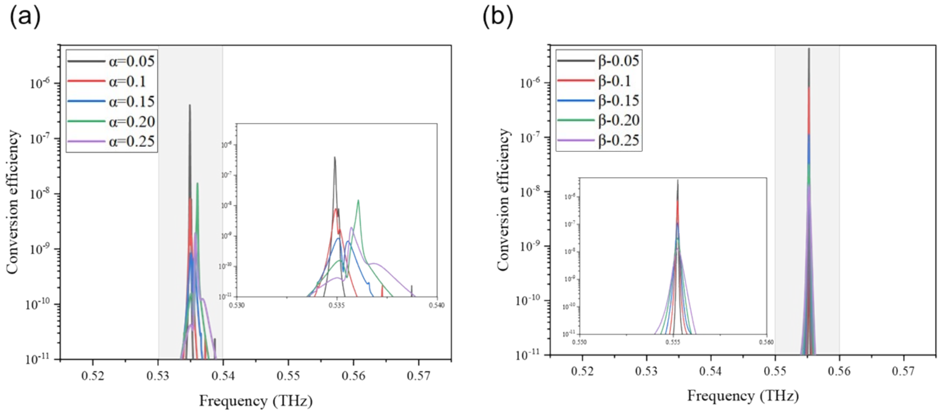

Figure S7 The conversion efficiency of THG under normal incidence for (a) width perturbation and (b) Gap perturbation, respectively.

Figures S7a and S7b illustrate the nonlinear enhancement of Q-GMs and BZF-BICs under normal incidence across different degrees of asymmetry. Notably, a pronounced enhancement in conversion efficiency emerges exclusively at the Q-GM resonances. To elucidate this phenomenon, we analyze the light-matter interaction within the framework of nonlinear coupled-mode theory (CMT). Under the undepleted pump approximation, the dynamic evolution of the fundamental mode amplitude a inside the resonator driven by an incident pump wave Sin at frequency ω can be described by the CMT equation.

$$\frac{da}{dt} = \left(-i\omega_0 - \gamma_{\text{rad}} - \gamma_{\text{nr}}\right)a + \sqrt{2\gamma_{\text{rad}}}s_{\text{in}} \backslash* \quad \text{MERGEFORMAT}$$

(S44)

where ω_0 is the resonant frequency, γ_{rad} is the radiative leakage rate (input/output coupling rate to free space), and γ_{nrad} represents the intrinsic non-radiative decay rate. The term $\sqrt{2\gamma_{\text{rad}}}s_{\text{in}}$ denotes the input coupling term, which dictates how much external pump energy enters the resonator.

At steady state and under exact resonance condition ($\omega=\omega_0$), the internal mode energy $|\mathrm{a}|^2$ can be expressed as

$$|a|^2 = \frac{2\gamma_{\text{rad}}}{(\gamma_{\text{rad}} + \gamma_{\text{nr}})^2}|s_{\text{in}}|^2 \quad \backslash* \text{ MERGEFORMAT (S45)}$$

For a third-order nonlinear process, the nonlinear polarization driving the THG is proportional to the cube of the fundamental local field. Consequently, the generated third-harmonic power $P^{(3)}$ is proportional to $|\mathrm{a}|^6$. The overall THG conversion efficiency is therefore governed by the internal field enhancement.

$$\eta \propto \frac{|a|^6}{|s_{\text{in}}|^2} \propto \frac{\gamma_{\text{rad}}^3}{(\gamma_{\text{rad}} + \gamma_{\text{nr}})^6} P_{pump}^2 \backslash* \text{ MERGEFORMAT (S46)}$$

Based on this theoretical framework, an infinite Q-factor, such as that of an ideal

BZF-BIC under normal incidence, yields zero nonlinear conversion due to a total impedance mismatch ($\gamma_{\mathrm{rad}} = 0$). Instead, the maximum THG efficiency is strictly determined by the critical coupling condition. The fundamental advantage of Q-GMs lies in their ability to dynamically tune the radiative leakage via the geometric asymmetry parameter. By opening the radiative channel, Q-GMs resolve the input-coupling bottleneck inherent to dark BICs, allowing the system to operate in the optimal coupling regime and providing the strong THG enhancement observed in our full-wave simulations.Furthermore, because the radiative leakage rate of Q-GMs remains relatively stable across a broad momentum space, this highly efficient nonlinear enhancement can be maintained over a wide range of incident angles. In contrast, the radiative channels associated with angle-sensitive BICs fluctuate sharply with the incident angle, severely degrading the nonlinear conversion efficiency under oblique illumination.

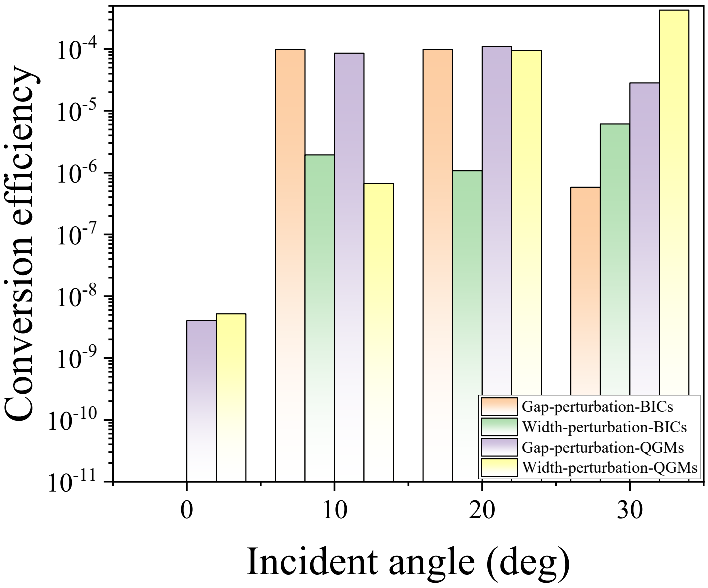

Figure S8 The dependence of peak THG efficiency on the incident angle.

To systematically evaluate the angular robustness of the proposed nonlocal metasurface, we investigated the peak THG conversion efficiency across a broad range of incident angles. As shown in Supplementary Figure S8, the THG maintains a high conversion efficiency from normal incidence up to large oblique angle. This sustained performance confirms that the nonlocal Brillouin zone folding (BZF) mechanism successfully flattens the Q-factor distribution in momentum space, establishing a robust enhancement.

Furthermore, this systematic analysis clarifies the interplay between the broad Q-GM enhancement and the narrow accidental-BIC-induced peaks. While the Q-GM mechanism provides the characteristic alignment-tolerant performance, accidental

BICs exist as isolated topological singularities at specific angle-frequency coordinates. In the immediate vicinity of these accidental BICs, the system can achieve even more extreme local field confinement, leading to THG spikes that further boost the efficiency beyond the baseline at accidental BICs. The coexistence of a stable Q-GM enhancement baseline and these high-sensitivity accidental-BIC peaks underscores the versatility of our design for both robust and extreme nonlinear photonic applications.

S7. The robustness of the nonlocal metasurfaces against fabrication imperfections

For practical fabricated devices, always introduce the inevitable fabrication defects. The nonlocal metasurfaces we proposed exhibit a certain level of robustness to variations of the grating shape. As shown in Figure S9. The nonlocal metasurfaces still exhibit strong electric field localization in the structure when we chamfer the regular rectangular grating. As shown in Figure S9 (b) (e), The position of the resonance peak and the full width at half maximum only have slight changes, and the resonance characteristics basically remain compared to the traditional rectangular grating. The electric field confirms the resonance results shown in Figure S9 (d) (e). Hence, it can be concluded that the robustness to shape ensures that any structural errors introduced during fabrication will not significantly impact the spectral response. This characteristic proves highly beneficial for experimental production purposes.

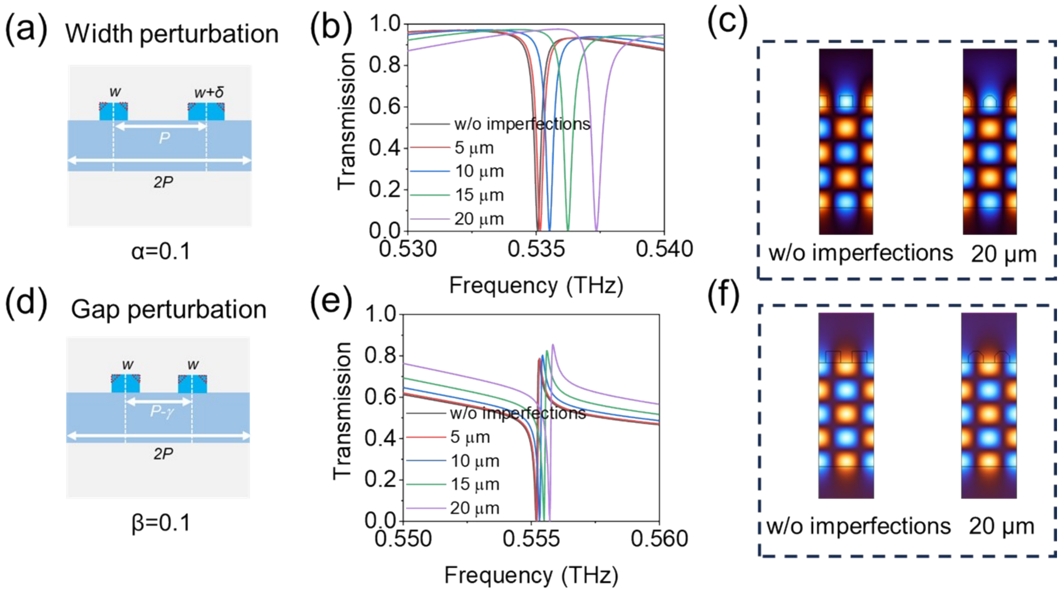

Figure S9 Robustness of the proposed nonlocal metasurfaces. (a) and (c) Schematic diagram where the side wall of the grating structure is not vertical, and the chamfer length is represented by the right sides of the red dotted triangle with width perturbation or gap perturbation, respectively. (b) and (e) The transmission spectrum with different chamfer lengths with width perturbation or gap perturbation, respectively. (e) and (f) The electric field under different chamfer lengths with width perturbation or gap perturbation, respectively

Reference

1. W. Shi, J. Gu, X. Zhang, Q. Xu, J. Han, Q. Yang, L. Cong and W. Zhang, Terahertz bound states in the continuum with incident angle robustness induced by a dual period metagrating. Photonics Research **10** (3), 810-819 (2022).
2. A. C. Overvig, S. Shrestha and N. Yu, Dimerized high contrast gratings. Nanophotonics **7** (6), 1157-1168 (2018).
3. G. Gallot, S. P. Jamison, R. W. McGowan and D. Grischkowsky, Terahertz waveguides. Journal of the Optical Society of America B **17** (5), 851-863 (2000).
4. W. Wang, Y. K. Srivastava, T. C. Tan, Z. Wang and R. Singh, Brillouin zone folding driven bound states in the continuum. Nature Communications **14** (1), 2811 (2023).
5. W. Ye, Y. Gao and J. Liu, Singular Points of Polarizations in the Momentum Space of Photonic Crystal Slabs. Physical Review Letters **124** (15), 153904 (2020).
6. M. Kang, L. Mao, S. Zhang, M. Xiao, H. Xu and C. T. Chan, Merging bound states in the continuum by harnessing higher-order topological charges. Light: Science & Applications **11** (1), 228 (2022).
7. S. You, M. Zhou, L. Xu, D. Chen, M. Fan, J. Huang, W. Ma, S. Luo, M. Rahmani, C. Zhou, A. E. Miroshnichenko and L. Huang, Quasi-bound states in the continuum with a stable resonance wavelength in dimer dielectric metasurfaces. Nanophotonics **12** (11), 2051-2060 (2023).
8. N. K. Hon, R. Soref and B. Jalali, The third-order nonlinear optical coefficients of

Si, Ge, and Si1−xGex in the midwave and longwave infrared. Journal of Applied Physics **110** (1) (2011).

9. G. Sun, Y. Wang, Z. Cui, R. Xie and X. Zhao, Enhanced terahertz high-harmonic generation from high-Q quasi-bound states in the continuum empowered by permittivity-broken metasurface. Applied Physics Letters **124** (11) (2024).